J. Fluid Mech. (2007), *vol.* 590, *pp.* 163–185.
doi:10.1017/S0022112007007975 Printed in the United Kingdom

The full impulse response of two-dimensional jet/wake flows and implications for confinement

MATTHEW P. JUNIPER

Department of Engineering, University of Cambridge,
Trumpington Street, Cambridge, CB2 1PZ, UK

(Received 5 October 2006 and in revised form 19 June 2007)

In this theoretical study, a linear spatio-temporal analysis is performed on unconfined and confined inviscid jet/wake flows in order to determine whether they are absolutely or convectively unstable. The impulse response is evaluated in the entire outer fluid, rather than just at the point of impulse, over a wide range of density ratios. This confirms that the dominant saddle point can validly migrate into the plane of diverging eigenfunctions. This reveals that, at certain density ratios and shear numbers, the response can grow upstream in some directions with a cross-stream component, even though it decays directly upstream of, and at, the point of impulse. This type of flow is convectively unstable when unconfined, but becomes absolutely unstable when confined. Other effects of confinement are described in a previous paper. Together, these articles have important implications for the design of fuel injectors, which often employ confined shear flows at high Reynolds number and large density ratios to generate strong mixing in combustion chambers.

1. Introduction

This article examines the stability of unconfined and confined jets and wakes over a large range of density ratios. It identifies a previously unrecognized region of this parameter space that has important implications for confined flows. The model consists of a central sheet of one fluid sandwiched between two identical sheets of another fluid. If the inner fluid moves faster than the outer fluid, it is a jet flow. If the outer fluid moves faster than the inner fluid, it is a wake flow. This model is similar to that studied by Yu & Monkewitz (1990). The impulse response is calculated with a linear spatio-temporal instability analysis. In a new development for jets and wakes, the growth rate is calculated in the entire outer fluid, rather than just at the point of impulse. Particular attention is paid to the shape of the impulse and the group and phase velocities of the growing eigenmodes.

Juniper (2006) performed a spatio-temporal stability analysis on unconfined jets and wakes and found that, for certain density and velocity ratios, the eigenmode with zero group velocity could have a purely imaginary wavenumber. In that paper, these eigenmodes were discounted on the grounds that they would have infinite wavelength in the streamwise direction and therefore violate the WKBJ assumption. However, Healey (2006) found the same type of eigenmode in a rotating disk boundary layer and showed that they are permissible and that they represent growth and propagation in the cross-stream direction. One aim of the present paper is to re-examine unconfined jets and wakes, without discounting these eigenmodes, to discover

whether the behaviour that Healey discovered in a rotating disk boundary layer also occurs in jets and wakes.

In related work on confined jets and wakes, Juniper (2006) explained why these flows are particularly unstable when the inner and outer fluids have similar thicknesses. This study also predicted that the instability characteristics of confined flows do not tend to those of unconfined flows, even when the confining plates are very far away. This matter was not resolved in that paper and the saddle points that represented the eigenmodes of this instability were called 'ambiguous'. However, Healey (2007) found the same type of saddle point in a confined rotating disk boundary layer and showed that they do have physical significance. A second aim of the present paper is to re-examine confined jets and wakes and remove the ambiguity regarding these saddle points in jets and wakes.

For inviscid flow, the theoretical study of Juniper & Candel (2003) has shown that jets and wakes become absolutely unstable over a wider range of shear when they are confined. The full background to this problem and its practical implications are explained in that paper and are not repeated here. The physical reason for this behaviour has been explained by Juniper (2006). The same technique can be used to show that a Rankine vortex with axial flow becomes particularly unstable to the $m=1$ mode when confined. This is in agreement with the large eddy simulations of Garcia-Villalba, Fröhlich & Rodi (2006) at a Reynolds number of 81 500. These simulations show the existence of this large-scale helical mode for a confined flow, but no large coherent structures in the equivalent unconfined flow. These results are relevant to fuel injection in rockets and aircraft, where these coherent structures aid mixing in the combustion chamber and improve combustion efficiency (Barrère *et al.* 1960).

On the other hand, confinement seems to have a stabilizing effect on viscous flow at Reynolds numbers between 40 and 140. Experiments by Shair *et al.* (1963) and numerical simulations by Chen, Pritchard & Tavener (1995) have shown that vortex shedding behind a cylinder starts at a higher Reynolds number when the cylinder is confined within a duct. Furthermore, once vortex shedding has started, Delbende & Chomaz (1998) show that confinement damps the secondary pairing instability of the shed vortices.

One of the key features of this analysis is its simplicity. The model described in § 2 contains all the features that need to be examined, but its dispersion relation remains explicit, which greatly simplifies the subsequent analysis. A further simplification would be to omit the finite-thickness shear layers between the flows. However, the finite thickness is required because the associated saddle point provides the selection criterion for the saddle points associated with the interaction of the two shear layers. For most of this paper the shear layer is very thin and the exact velocity profile has little influence on the latter mode. Therefore the piece-wise linear velocity profile is sufficiently accurate. Even when the shear layer is thick, Esch (1957) demonstrates that the stability of this piece-wise linear velocity profile is reasonably close to that of a realistic velocity profile.

A linear spatio-temporal stability analysis is used in § 3 because this is quicker than a nonlinear analysis but has been shown by Delbende & Chomaz (1998) to be a good predictor of nonlinear behaviour in similar flows. As in Healey (2006), the growth of the impulse response is examined in the whole outer fluid, rather than just at the point of impulse. Although Delbende & Chomaz (1998) have calculated the impulse response in the outer fluid with direct numerical simulation, the advantage of the current method is that the stability characteristics of flows can be calculated much

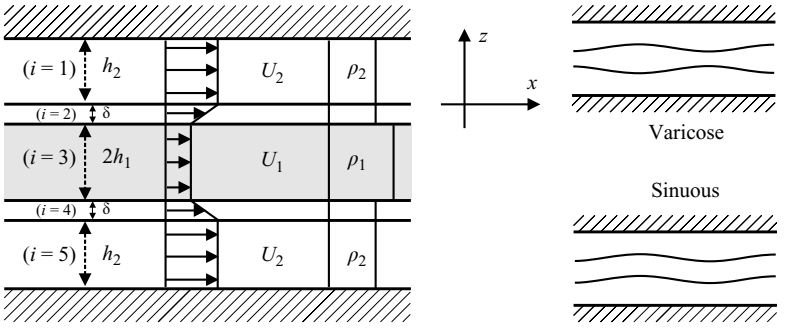

FIGURE 1. The model consists of three uniform inviscid flows separated by two shear layers with linear velocity profiles. The flows have infinite extent in the x-direction and are uniform in the y-direction. The x-axis is at the interface of fluids 1 and 2. Only varicose and sinuous perturbations are examined.

more rapidly over a wider range of parameter values. It is particularly interesting to study a wide range of density ratios.

The advantage of the analytic linear analysis becomes evident in § 4, where saddle points in the k-plane are easily located and then distinguished by both their physical relevance and their influence on the impulse response. In § 5, it is shown that one of these saddle points can legitimately cross the k_i-axis, with important consequences for the shape of the impulse response in the outer fluid. This allows the stability of jets and wakes to be characterized in terms of density ratio and shear number in § 6. In one region of this parameter space, the impulse response can grow upstream in some directions with a cross-stream component, even though it decays directly upstream of, and at, the point of impulse. This curious behaviour has important implications for confined flows, as described in § 7.

2. Derivation of the model's dispersion relation

The model (figure 1) consists of three uniform inviscid incompressible irrotational flows separated by two shear layers with linear velocity profiles. The inner flow has density ρ_1, velocity U_1 and thickness $2h_1$ in the z-direction. The outer flows both have density ρ_2 and velocity U_2. If unconfined, the outer flow extends to infinity in the z-direction. If confined, it has thickness h_2 in the z-direction. The shear layers both have thickness δ in the z-direction, density ρ_2 and linear velocity profiles, taking values between U_1 at the boundary with the inner fluid and U_2 at the boundary with the outer fluid. The flows have infinite extent in the x-direction and are uniform in the y-direction into the page.

Following Drazin & Reid (1981, § 21), normal mode perturbations of the form $\boldsymbol{u}(z)\exp(\mathrm{i}(k_x x + k_y y - \omega t))$ are introduced, where k_x and k_y are the wavenumbers in the x- and y-directions and ω is the angular frequency. This three-dimensional problem is reduced to an equivalent two-dimensional problem by introducing the wavenumber $\xi \equiv (k_x^2 + k_y^2)^{1/2}$.

In the complex k_x-plane, ξ has branch points at $k_x = \pm \mathrm{i}k_y$ and $k_x = \pm\infty$. The choice of branch cuts is discussed in the next two paragraphs because it has important consequences for the subsequent analysis. In § 3, a function will be integrated from $k_x = -\infty$ to $k_x = +\infty$ and it is convenient for the integration path to pass continuously between the branch points at $\pm \mathrm{i}k_y$ without encountering a branch cut. There is a

second set of branch points along the k_i-axis (figure 3*b*). The integration path cannot be deformed through a branch point so the branch cut from the branch point at $\mathrm{i}k_y$ must connect to a branch point in the $k_i > 0$ half-plane and the branch cut from the branch point at $-\mathrm{i}k_y$ must connect to a branch point in the $k_i < 0$ half-plane. The exact path of the branch cuts is fixed by the choice of the root of $(k_x^2 + k_y^2)^{1/2}$ at a particular value of k_x. Conventionally, the branch cuts would lie on the k_i-axis, but in § 5 the lower branch cut will be shifted off this axis.

The bulk flow has zero velocity in the y-direction so, by Squire's theorem, the most unstable perturbation is found when k_y tends to zero. The wavenumber in the y-direction has been mentioned in order to emphasize that the integration in the k_x-plane is continuous at $k_x = 0$. From now on, the infinitesimally small wavenumber k_y will be omitted and k_x will be replaced by k. This means that ξ tends to the positive or negative root of $(k^2)^{1/2}$. In Juniper (2006), this is written as $\pm sk$, where s is the sign of $\mathrm{Re}\{k\}$. However, the sign function pins the branch cuts to the k_i-axis and in this paper, ξ is retained so that the branch cuts can be shifted.

For the two-dimensional problem, perturbation streamfunctions of the form $\psi_i(x, z, t) = \varphi_i(z; \xi)\mathrm{e}^{\mathrm{i}(kx - \omega t)}$ can be defined in each flow such that the perturbation velocities are $u_x = \partial\psi_i/\partial z$ and $u_z = -\partial\psi_i/\partial x$. For future equations, e.g. (3.5), it is important to remember that φ_i is a function of ξ and hence k. However in this section, where normal modes are considered separately, it becomes a function only of z because k is held constant. The streamfunctions automatically satisfy continuity. To satisfy irrotationality they must also satisfy $\varphi_i'' - \xi^2\ \varphi_i = 0$. Convenient forms for φ_i in the top three flows are:

$$\varphi_1 = A\mathrm{e}^{+\xi z} + B\mathrm{e}^{-\xi z}, \tag{2.1}$$

$$\varphi_2 = C\cosh\xi(z+\delta) + E\sinh\xi(z+\delta), \tag{2.2}$$

$$\varphi_3 = F\cosh\xi(z+h_1+\delta) + G\sinh\xi(z+h_1+\delta). \tag{2.3}$$

Flows 4 and 5 do not need to be considered because this paper examines only varicose disturbances (where $F = 0$ and the velocity perturbations are symmetric about the central fluid) and sinuous disturbances (where $G = 0$ and the velocity perturbations are antisymmetric about the central fluid). Any perturbation can be made up from a linear combination of a varicose and a sinuous perturbation.

At $z = -\delta$ and $z = 0$, the kinematic and dynamic matching conditions between the flows are:

$$\Delta\left[\frac{\varphi}{(U - \omega/k)}\right] = 0, \tag{2.4}$$

$$\Delta[\rho(U - \omega/k)\varphi' - \rho U'\varphi] = 0. \tag{2.5}$$

There is a further kinematic boundary condition at the top of the outer flow, but it is more useful to apply this later and to leave an extra parameter A/B in the dispersion relation for the moment. This allows convergent eigenfunctions and divergent eigenfunctions to be clearly distinguished, which is important for the rest of this paper.

For varicose or sinuous perturbations there are five unknowns and four equations. After long but elementary manipulation, these can be reduced to one equation which contains the unknown parameter A/B:

$$D \equiv A \times D^- + B \times D^+ = 0, \tag{2.6}$$

where, for varicose perturbations:

$$D^- \equiv (V_1\xi\delta(\rho_1/\rho_2)\coth\xi h_1 + 1)(V_2\xi\delta(\cosh\xi\delta + \sinh\xi\delta) - \sinh\xi\delta) + V_1\xi\delta(V_2\xi\delta(\cosh\xi\delta + \sinh\xi\delta) - \cosh\xi\delta), \tag{2.7}$$

$$D^+ \equiv (V_1\xi\delta(\rho_1/\rho_2)\coth\xi h_1 + 1)(V_2\xi\delta(\cosh\xi\delta - \sinh\xi\delta) - \sinh\xi\delta) - V_1\xi\delta(V_2\xi\delta(\cosh\xi\delta - \sinh\xi\delta) + \cosh\xi\delta), \tag{2.8}$$

with $V_1 \equiv (U_1 - \omega/k)/(U_2 - U_1)$ and $V_2 \equiv (U_2 - \omega/k)/(U_2 - U_1)$. For sinuous perturbations $\coth\xi h_1$ is replaced by $\tanh\xi h_1$.

In the confined case, the ratio A/B is equal to $-\exp(-2\xi h_2)$ owing to the boundary condition of zero z-velocity at $z = h_2$. If ξ is defined as the positive root of $(k^2)^{1/2}$, then the ratio A/B lies in the range $-1 \leqslant A/B < 0$ and the A-term in (2.1) corresponds to eigenfunctions that grow in the positive z-direction (divergent eigenfunctions) and the B-term corresponds to eigenfunctions that decay in the positive z-direction (convergent eigenfunctions). On the other hand, if ξ is defined as the negative root of $(k^2)^{1/2}$ then the ratio lies in the range $-\infty < A/B \leqslant -1$ and the A-term corresponds to convergent eigenfunctions and the B-term corresponds to divergent eigenfunctions. Neither A nor B can equal zero so the confined solution is always a linear combination of divergent and convergent eigenfunctions and the dispersion relation (2.6) is always a linear combination of D^- and D^+.

In the unconfined case, either A or B must equal zero because, by the previous argument, any superposition of divergent and convergent eigenfunctions must correspond to a confined case. With ξ defined as the positive root of $(k^2)^{1/2}$, either A is set to zero and $D^+ = 0$ is solved on the plane of converging eigenfunctions (the B-plane) or B is set to zero and $D^- = 0$ is solved on the plane of diverging eigenfunctions (the A-plane). The physical solution lies on the B-plane because converging eigenfunctions satisfy the boundary condition of zero z-velocity at $z \to \infty$ and diverging eigenfunctions do not. The opposite is true if ξ is defined as the negative root of $(k^2)^{1/2}$.

In the rest of this section and in § 3, ξ is defined as the positive root of $(k^2)^{1/2}$. In § 3, the impulse response is evaluated by integrating solutions of the dispersion relation from $k = -\infty$ to $+\infty$. The preceding paragraphs have shown why, for the unconfined case, this integration should be performed over solutions of $D^+ = 0$ on the B-plane of converging eigenfunctions. In §§ 4 and 5, it is shown that the integration is easier to evaluate if the branch cut on the k_i-axis is shifted so that the integration path passes into a small region where $\mathrm{Re}\{\xi\}$ is negative. It is important to note that integration over this small region of divergent eigenfunctions is not the same as integration over the A-plane of divergent eigenfunctions because the solutions on the path continue to satisfy $D^+ = 0$ rather than $D^- = 0$. This process of shifting the branch cut simply provides an easier way to perform the integral in the B-plane. Integration with $D^- = 0$ over the A-plane always remains unphysical. In practice, this process is achieved by replacing ξ with k and then ensuring that the integration path passes back round the branch point at $-\mathrm{i}k_y$.

A Taylor expansion can be performed on (2.7) and (2.8) in the thin shear-layer limit, $\xi\delta \to 0$. Retaining the second-order terms, D^- and D^+ tend to:

$$D^- \equiv \rho_1(U_1 - \omega/k)^2\coth(\xi h_1) - \rho_2(U_2 - \omega/k)^2, \tag{2.9}$$

$$D^+ \equiv \rho_1(U_1 - \omega/k)^2\coth(\xi h_1) + \rho_2(U_2 - \omega/k)^2. \tag{2.10}$$

In the confined case, where $A/B = -\exp(-2\xi h_2)$, the dispersion relation becomes:

$$D \equiv \rho_1(U_1 - \omega/k)^2 \coth(\xi h_1) + \rho_2(U_2 - \omega/k)^2 \coth(\xi h_2) = 0. \tag{2.11}$$

These are the same as the dispersion relations derived via a different method by Juniper (2006).

It is convenient to introduce a non-dimensional framework and the following reference scales: velocity, $U_{ref} \equiv (U_1 + U_2)/2$; length, h_1; density, ρ_2. The dimensionless variables are $\omega^* \equiv \omega h_1/U_{ref}$, $k^* \equiv k h_1$ and $\xi^* \equiv \xi h_1$. The dimensionless parameters are $\Lambda \equiv (U_1 - U_2)/(U_1 + U_2)$, $S \equiv \rho_1/\rho_2$, $h \equiv h_2/h_1$ and $\delta^* \equiv \delta/h_1$. The dispersion relations for unconfined and confined varicose perturbations when $\xi^*\delta^*$ tends to zero are, respectively:

$$D^{+*} \equiv S(1 + \Lambda - \omega^*/k^*)^2 \coth(\xi^*) + (1 - \Lambda - \omega^*/k^*)^2 = 0, \tag{2.12}$$

$$D^* \equiv S(1 + \Lambda - \omega^*/k^*)^2 \coth(\xi^*) + (1 - \Lambda - \omega^*/k^*)^2 \coth(\xi^* h) = 0. \tag{2.13}$$

In the rest of this paper the non-dimensional framework will be used and the asterisks will be dropped. It is conventional to use Λ as the shear parameter. However, the parameter $1/\Lambda$ is used for figures in this paper because this allows absolutely unstable regions to be plotted as single regions in parameter space.

3. Spatio-temporal instability analysis in the outer fluid

Most spatio-temporal instability analyses examine the response at a point in space to an impulse at the same point in space. If this response grows in time, then the flow is absolutely unstable. If it decays, then the flow is either convectively unstable or stable. In this paper, the response is examined throughout the outer fluid. When a perturbation develops and grows at the shear layer, it also propagates and grows in the outer fluid. However, it is important to point out that this propagation and growth is merely a kinematic response to the perturbation at the shear layer.

The case with real k is quite familiar, consisting of travelling waves with constant amplitude in the x-direction and waves with exponentially decaying amplitude in the z-direction. The case with complex k is less familiar, consisting of travelling waves with constant amplitude at an angle to the x-axis and exponential decay perpendicular to this angle. Examination of the modes that propagate and grow in the outer fluid gives a much clearer picture of the impulse response than examination simply at the point of impulse.

The aims of this section are to show how the impulse response is calculated in the outer fluid, to describe the shape of the impulse that excites all modes equally, to explain why its response is equivalent to that of a point source impulse and briefly to describe the characteristics of the response by considering the group velocity in the outer fluid.

3.1. *The one-dimensional response*

A conventional analysis, such as that in Huerre (2000), is performed in one spatial dimension. The (x, t)-dependence of the perturbation streamfunction defined in § 2 is expressed as the double Fourier integral of its normal mode perturbations:

$$\psi_i(x, t) = \frac{1}{(2\pi)^2} \int_{F_k} \int_{L_\omega} \hat{\psi}_i(k, \omega) \mathrm{e}^{\mathrm{i}(kx - \omega t)} \, \mathrm{d}\omega \, \mathrm{d}k. \tag{3.1}$$

By substituting for k and ω, the dispersion relation $D(k, \omega)$ can be expressed as a differential operator that relates the perturbation streamfunction $\psi_i(x, t)$ to the

forcing $S_i(x,t)$:

$$D\left(-\mathrm{i}\frac{\partial}{\partial x}, \mathrm{i}\frac{\partial}{\partial t}\right)\ \psi_i(x,t) = S_i(x,t). \tag{3.2}$$

The forcing can also be expressed as the double Fourier integral of its normal modes:

$$S_i(x,t) = \frac{1}{(2\pi)^2}\int_{F_k}\int_{L_\omega} \hat{S}_i(k,\omega)\mathrm{e}^{\mathrm{i}(kx-\omega t)}\,\mathrm{d}\omega\,\mathrm{d}k. \tag{3.3}$$

Substituting (3.1) and (3.3) into (3.2) gives the governing equation in spectral space:

$$\hat{\psi}_i(k,\omega)D(k,\omega) = \hat{S}_i(k,\omega). \tag{3.4}$$

If the forcing streamfunction is $S_i(x,t)=\delta(x)\delta(t)$ then $\hat{S}_i(k,\omega)=1$ and $\psi(x,t)$ is the impulse response. It is evaluated by substituting (3.4) into (3.1) and following the procedure described in § 3.4.

3.2. *The two-dimensional response*

The full impulse response is evaluated in two spatial dimensions. Each mode of the perturbation streamfunction is of the form $\psi_i(x,z,t)=\varphi_i(z;\xi)\mathrm{e}^{\mathrm{i}(kx-\omega t)}$, where the functions $\varphi_i(z;\xi)$ are given by (2.1) to (2.3). The full streamfunction, evaluated at all values of z, is the double Fourier integral of the normal mode perturbations in (3.1) multiplied by the mode shapes $\varphi_i(z;\xi)$:

$$\psi_i(x,z,t) = \frac{1}{(2\pi)^2}\int_{F_k}\int_{L_\omega} \hat{\psi}_i(k,\omega)\varphi_i(z;\xi)\mathrm{e}^{\mathrm{i}(kx-\omega t)}\,\mathrm{d}\omega\,\mathrm{d}k. \tag{3.5}$$

If the forcing excites all modes equally at $(x,t)=(0,0)$ then the full forcing is the double Fourier integral of the normal modes in (3.3) multiplied by the same mode shapes:

$$S_i(x,z,t) = \frac{1}{(2\pi)^2}\int_{F_k}\int_{L_\omega} \hat{S}_i(k,\omega)\varphi_i(z;\xi)\mathrm{e}^{\mathrm{i}(kx-\omega t)}\,\mathrm{d}\omega\,\mathrm{d}k. \tag{3.6}$$

The response and the forcing are still related by (3.2) at $z=0$. Substituting (3.5) and (3.6) into this equation gives the same spectral governing equation as the one-dimensional case (3.4), whether or not the z-dependence is included. Therefore the response in two dimensions is also evaluated by substituting (3.4) into (3.5) and following the procedure described in § 3.4.

3.3. *The two-dimensional impulse*

If the impulse is concentrated at a point in the x-direction, then $\hat{S}_i(k,\omega)=1$. However, this impulse is not restricted to a point in the z-direction because it has been forced to satisfy $\nabla^2 S_i = 0$ through the imposition of the mode shapes $\varphi(z;\xi)$ in (3.6). Substituting (2.1) with $A=0$ into (3.6) gives the shape of this impulse in the outer fluid:

$$\begin{aligned} S_1(x,z,t) &= \frac{1}{(2\pi)^2}\int_{F_k}\int_{L_\omega} \mathrm{e}^{-\xi z}\mathrm{e}^{\mathrm{i}(kx-\omega t)}\,\mathrm{d}\omega\,\mathrm{d}k \\ &= \frac{\delta(t)}{2\pi}\int_{-\infty}^{0} \mathrm{e}^{kz}\mathrm{e}^{\mathrm{i}kx}\,\mathrm{d}k + \frac{\delta(t)}{2\pi}\int_{0}^{\infty} \mathrm{e}^{-kz}\mathrm{e}^{\mathrm{i}kx}\,\mathrm{d}k \\ &= \frac{\delta(t)}{\pi}\frac{z}{x^2+z^2}. \end{aligned}$$

This is a doublet. At $z=0$ it is equal to $\delta(x)\delta(t)$, but at $z\neq 0$ it is spread out, although it still integrates to 1 in the x-direction. The response from this doublet impulse is the same as the response from a point impulse, as demonstrated below.

In the bulk of the fluid, $z \neq 0$, the response $\psi_i(x,z,t)$ is related to the forcing $S_i(x,z,t)$ by the two-dimensional equivalent of (3.2):

$$D\ \psi_i(x,z,t) = S_i(x,z,t) \quad \text{for } z \neq 0. \tag{3.7}$$

The only constraints on the fluid are that it is irrotational and incompressible. There are no dynamic constraints because the pressure perturbation is unconstrained, except at $z=0$. The operator D is therefore equal to ∇^2 for $z \neq 0$.

If the forcing is an impulse at $t=0$, then the response in the bulk fluid at $t>0$ is governed by $\nabla^2\psi_i = 0$. There is no time dependence in the operator and therefore the solution at $t>0$ depends only on the kinematic boundary conditions of the bulk fluid. In other words, at $t>0$, the bulk fluid has no memory of the impulse that was in the bulk fluid, except through the impulse's effect on the shear layer at $z=0$. However, the response at the shear layer, $z=0$, depends only on the forcing at $z=0$, as shown in § 3.2.

This means that the response from a point impulse $S(x,z,t) = \delta(x)\delta(z)\delta(t)$ will be the same as that from any impulse that satisfies $S(x,0,t) = \delta(x)\delta(t)$. The doublet impulse satisfies this condition so its response is the same as that from a point impulse.

As an aside, if the doublet impulse were applied away from the shear layer, it would still excite every mode $\hat{S}(k,\omega)$ at the shear layer, although not with equal amplitude. This would not matter in this paper because the rest of this analysis is concerned with growth rates of normal modes rather than their absolute amplitudes. This is unlike the point impulse which, within the restrictions of the current model, would not excite any modes if it were applied inside the bulk fluid.

3.4. *Evaluation of the double Fourier integral*

The residue theorem is applied to (3.5) in order to perform the integration in ω (thus eliminating the functions that are excited by the impulse, but that do not satisfy $D(k,\omega)=0$). For each value of k, two values of ω satisfy $D(k,\omega)=0$ so there are two separate integrals:

$$\begin{aligned}\psi_i(x,z,t) = &-\frac{\mathrm{i}}{2\pi}\int_{F_k} \frac{\varphi_i(z;\xi)}{(\partial D/\partial\omega)[k,\omega_1(k)]}\exp(\mathrm{i}[kx-\omega_1(k)t])\,\mathrm{d}k \\ &-\frac{\mathrm{i}}{2\pi}\int_{F_k} \frac{\varphi_i(z;\xi)}{(\partial D/\partial\omega)[k,\omega_2(k)]}\exp(\mathrm{i}[kx-\omega_2(k)t])\,\mathrm{d}k.\end{aligned} \tag{3.8}$$

The solutions are symmetric under the transformation $\mathrm{Re}\{\omega_1,k_1\} \leftrightarrow -\mathrm{Re}\{\omega_2,k_2\}$, which results in the integration paths and the ω-planes being mirror images of each other in the k_i- and ω_i-axes. Consequently, the integrals from $-\infty \leqslant k \leqslant \infty$ are identical and the impulse response can be found by evaluating just one of the integrals in (3.8).

The response in the outer fluid is evaluated by substituting (2.1) into (3.8), as performed by Healey (2006) for the rotating disk boundary layer. Following the argument in § 2, the integral is calculated on the B-plane, where $A=0$:

$$\psi_1(x,z,t) = -\frac{\mathrm{i}}{2\pi}\int_{F_k} \frac{B}{(\partial D/\partial\omega)[k,\omega(k)]}\mathrm{e}^{-\mathrm{i}gt}\,\mathrm{d}k \quad \text{where } g \equiv [\omega(k) - \mathrm{i}\xi z/t - kx/t]. \tag{3.9}$$

The response is best visualized by plotting contours of the growth rate, g_i, in the $(x/t, z/t)$-plane. The procedure is described in § 4. These contours are shown in

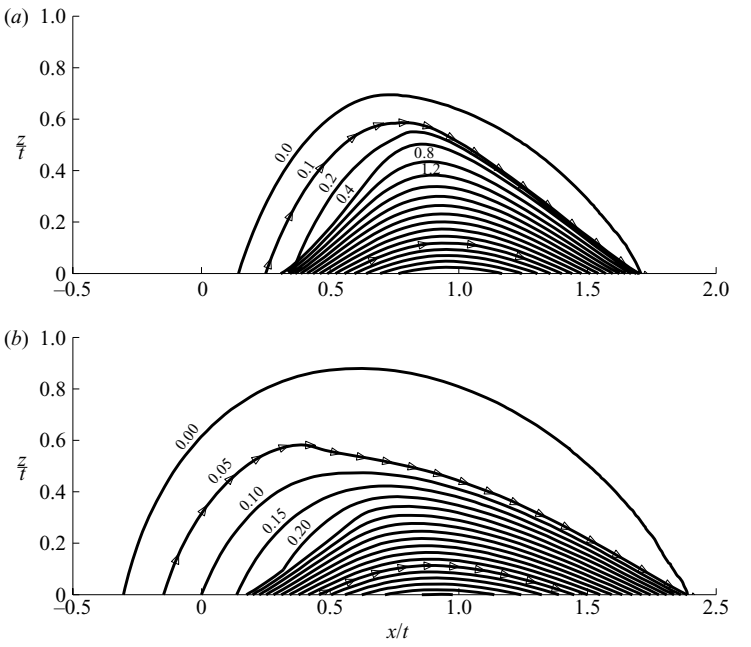

FIGURE 2. Examples of the impulse responses in the outer fluid of an unconfined flow, shown as contours of the growth rate of the most unstable saddle for varicose perturbations of (*a*) a convectively unstable flow at $(1/\Lambda, S, \delta) = (\sqrt{2}, 0.5, 0.05)$, for which $g_i(0,0) < 0$ and (*b*) an absolutely unstable flow at $(1/\Lambda, S, \delta) = (1.1, 0.1, 0.05)$, for which $g_i(0,0) > 0$. The mode that dominates at each point in the wavepacket has group velocity $(x/t, z/t)$ and phase velocity parallel to the contours of constant g_i, as shown by the arrows on selected contours.

figure 2. Examination of the response in the entire outer fluid of an unconfined flow gives more information than examination just at the point of impulse. This turns out to be crucial for the flows described in §§ 5 and 6.

3.5. *Group velocity, divergent eigenfunctions and phase velocity*

The flow is dispersive, which means that the different Fourier components of the response travel at different group velocities and, after some time, are found at different places. The mode observed in the vicinity of an observer who travels at constant x/t and z/t corresponds to the eigenmode with group velocity $(x/t, z/t)$. This eigenmode has a growth rate, g_i, and an associated eigenfunction $\varphi_i(z)$. It is important to note that this eigenmode does not occupy all space. In § 5, it will be shown that the eigenfunction is convergent (i.e. the amplitude decreases with increasing z) if the eigenmode at slightly higher z/t has a smaller growth rate and that the eigenfunction is divergent (i.e. the amplitude increases with increasing z) if the eigenmode at slightly higher z/t has a higher growth rate. At this stage it should be noted that a wavepacket can contain regions of divergent eigenfunctions without violating the boundary condition at $z = \infty$, as long as the eigenfunctions along its top perimeter are convergent.

As an aside, the direction of the wavevector is easily found. The dominant eigenmode at each point in the wavepacket consists of a series of wavecrests that travel in one direction and that grow and decay exponentially in the perpendicular directions. Consequently, the wavecrests' direction of travel (the direction of the phase velocity) lies parallel to the lines of constant growth rate in figure 2. This can be

verified by considering the complex wavenumber, k, of a mode at $(x/t, z/t)$. At a given t, and taking $\xi = k$, the growth rate, g is equal to $\omega - \mathrm{i}kz/t - kx/t$ and the response is therefore proportional to $\mathrm{e}^{\mathrm{i}k(x+\mathrm{i}z)}$. This has constant amplitude when $k_i x + k_r z$ is constant and constant phase when $k_r x - k_i z$ is constant. These are parallel to rays $(z/t)/(x/t) = -k_i/k_r$ and $(z/t)/(x/t) = k_r/k_i$, respectively. The wavecrests' direction of travel calculated via this method is shown on selected contours in figure 2 and does indeed run parallel to lines of constant g_i.

4. Evaluation of the integral and distinction between saddle points

The aims of this section are to show how the integral (3.9) is evaluated, to distinguish between the two types of saddle point that contribute to its behaviour and to introduce a quick method of evaluating the integral when the shear-layer thickness tends to zero.

The integration (3.9) is performed in the complex k-plane from $k = -\infty$ to $+\infty$. The integration path originally lies on the real axis but the integration is easier to evaluate if the path is shifted, without crossing any poles or branch points of $g(k)$, which lie at the same positions as those of $\omega(k)$. The integral can be evaluated numerically along any such path, which has the advantage that the plane of diverging eigenfunctions can be avoided if so desired. However, a more common approach is to consider the long time limit, where the dominant contribution comes from the neighbourhood of the highest value of g_i on the integration path.

The integration can be visualized by plotting contours of g_i in the complex k-plane (figure 3) and then choosing the path that has the lowest maximum value of g_i. The surface $g(k)$ is hyperbolic everywhere so this path always passes over one or more saddle points, which have the highest local values of g_i. Lines of constant g_r are followed across each saddle in order to avoid oscillations from the $\exp(\mathrm{i}g_r t)$ term. In general, the saddles do not have the same values of g_r, so the paths over adjacent saddles are joined at strongly negative values of g_i so that there is negligible contribution from these oscillating terms. The long time behaviour of the impulse response can then be inferred from the behaviour of the highest saddle on the integration path.

In figures 3(a) and 3(b), which are for varicose pertubations, the integration path passes over one saddle point, s_1, at large k_r and one or more saddle points, s_2, near the k_i-axis. The shear-layer thickness in figure 3(b) is ten times smaller than that in figure 3(a). The physical significance of these saddle points will be described shortly. As δ decreases, saddle s_1 moves to higher k_r and the integration path passes over more of the s_2 saddles. Consequently, the position of saddle s_1 dictates which of the s_2 saddles lie on the integration path. In this respect, it is similar to the saddle associated with surface tension in figure 3 of Juniper (2006). In figures 3(a) and 3(b), the long time behaviour is dominated by saddle s_{2a} because it has the highest value of g_i. However, saddle s_1 dominates at other parameter values and on other rays $(x/t, z/t)$.

Figure 3(c) is a magnification of figure 3(a) around $k = 0$. The branch points at $\pm\mathrm{i}k_y$ have been shifted slightly so that the integration path can be seen to pass between these branch points, down to a region of very low g_i, where g_r changes, and then over saddle s_{2a}. The path can also be shifted off the negative k_r-axis, although this is not important because g_i is always negative on this axis.

In figures 4(a) and 4(b), contours of the growth rates of the s_1 and s_{2a} saddles are shown in the $(x/t, z/t)$-plane for the same parameter values as figures 3(a) and 3(b). The contours of figure 4(b) are presented separately in figure 5 so that the

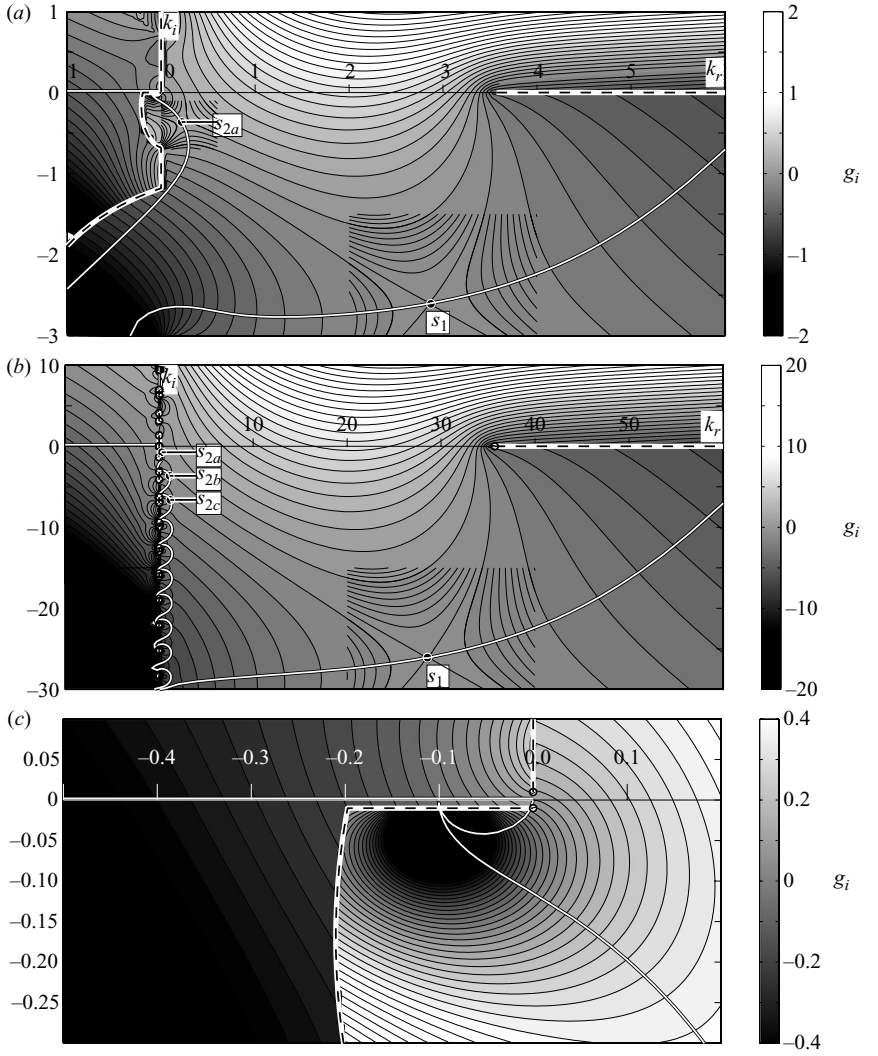

FIGURE 3. Contours of growth rate, g_i, in the complex k-plane along the ray $(x/t, z/t) = (0.2, 0.1)$ for varicose perturbations of an unconfined low-density jet flow, $(1/\Lambda, S) = (1.1, 0.1)$ with shear-layer thickness (*a*) $\delta = 0.5$ and (*b*) $\delta = 0.05$. The integration path (white line) passes over saddle s_1 and one or more of the s_2 saddles. In the long time limit, saddle s_{2a} dominates because it has the highest growth rate on the integration path. (*c*) is a magnification of (*a*) around the origin. Branch points are shown as white circles. In (*a*) and (*c*) the branch cuts have been shifted to show that the integration path passes between the branch points infinitesimally close to the origin (they are displaced by ± 0.01 so that the path can be seen) and then follows lines of constant g_r over the saddle points, changing to other values of g_r only when g_i is strongly negative.

contributions from the s_1 and s_{2a} saddles can be distinguished. It can be seen that the s_1 saddle contributes around the centre of the wavepacket and the s_{2a} saddle contributes to the bulge at the back. The s_{2b}, s_{2c} etc. saddles are never dominant at the values of δ in figures 4(*a*) and 4(*b*).

Physically, saddle s_1 is associated with the instability of each individual shear layer. A single shear layer (without surface tension) is never absolutely unstable to co-flow

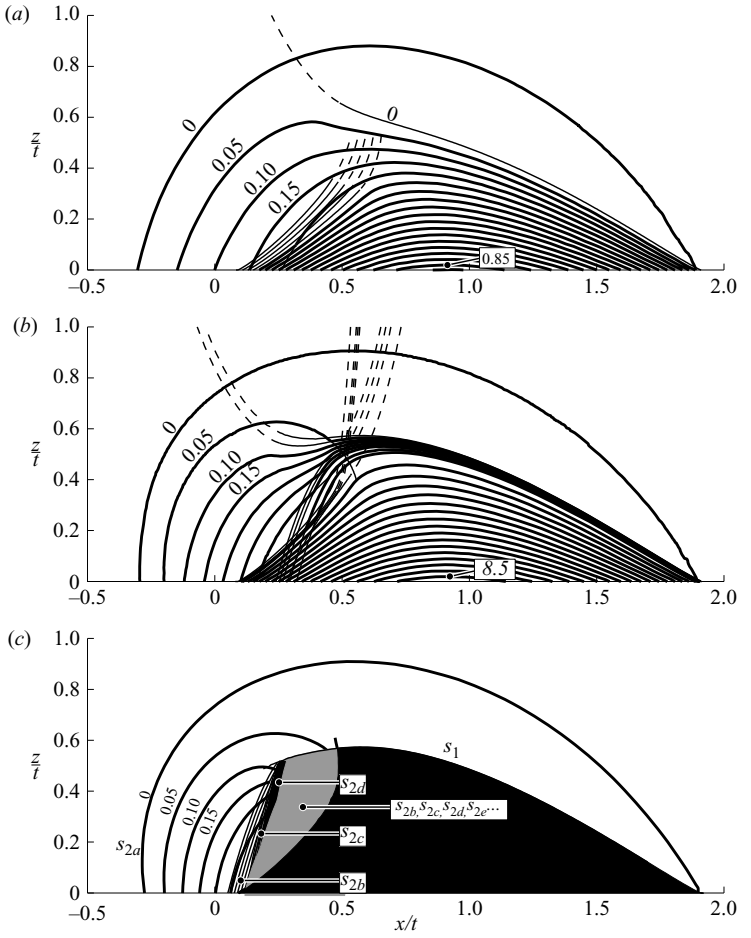

FIGURE 4. Contours of growth rate, g_i, in the $(x/t, z/t)$-plane for the same parameter values as figure 3 with (*a*) $\delta = 0.5$, (*b*) $\delta = 0.05$ and (*c*) $\delta \to 0$. In (*a*) and (*b*) the dominant saddle is shown as a thick solid line, subdominant saddles are shown as thin solid lines and saddles that have moved off the integration path are shown as thin dashed lines. The individual contours of (*b*) are broken down in figure 5 so that the contributions of saddles s_1 and s_{2a} can be distinguished. In (*c*) the thick lines show the growth rate of the s_{2a} saddle, the thin lines show the (subdominant) contours of the s_{2b}, s_{2c} etc. saddles, the solid black region shows where the s_1 saddle dominates and the grey region shows where the s_{2b}, s_{2c}, s_{2d} etc. saddles dominate.

($|1/\Lambda| > 1$) so the contribution from saddle s_1 is a region of growth that convects away from the source. For an infinitely thin shear layer, all wavelengths are unstable and their growth rates scale with k. For a finite-thickness shear layer, wavelengths lower than order δ are stabilized, so the highest growth rate scales with $1/\delta$, as can be seen by the fact that the maximum value of g_i in figure 4(*b*) is ten times greater than that in figure 4(*a*).

Physically, s_2 saddles are associated with the varicose motion of the two interacting shear layers. The varicose mode of saddle s_{2a} is responsible for the bulge that propagates and grows upstream at the back of the wavepacket. The growth rates and wavenumbers of this varicose mode are small but, nevertheless, cause absolute instability. As δ tends to zero, the growth rate contours asymptote to constant

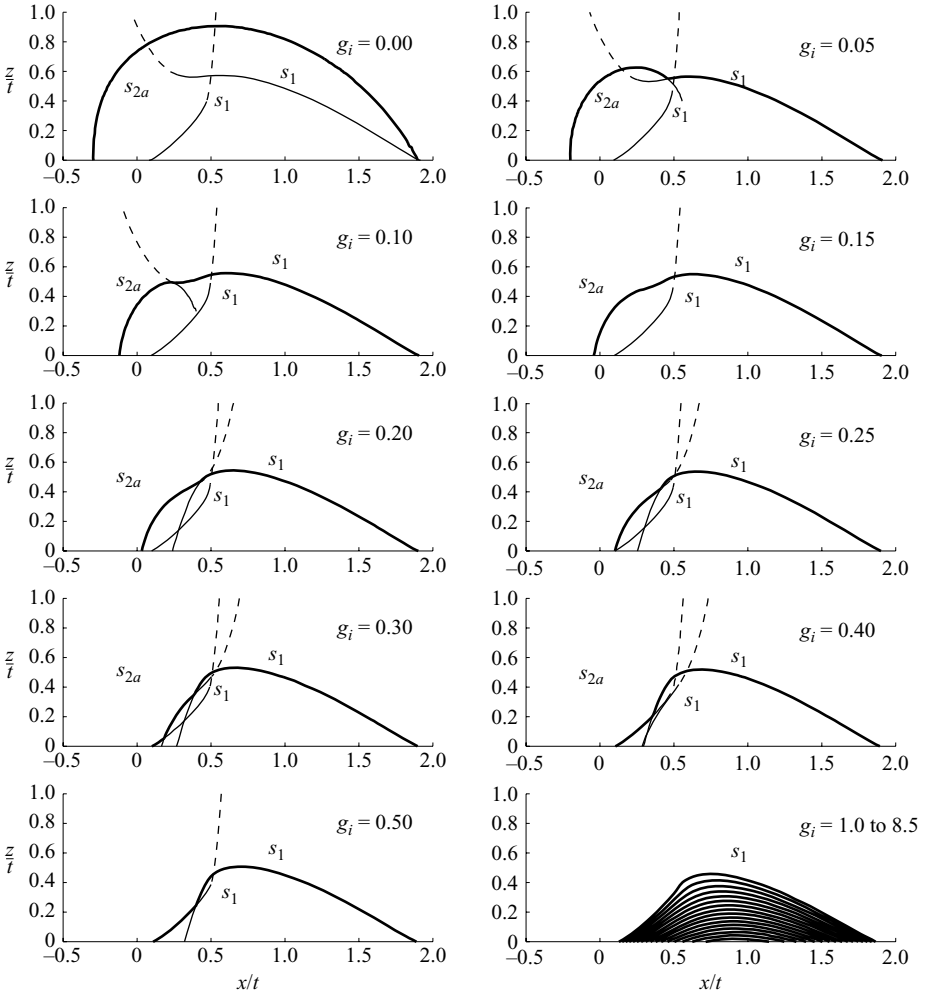

FIGURE 5. Breakdown of the contours in figure 4(*b*). At low g_i, saddle s_2 dominates at the back of the wavepacket and makes the flow absolutely unstable. This saddle is associated with the varicose motion of the interacting shear layers. At high g_i, saddle s_1 dominates, creating a region of strong convective instability at the centre of the wavepacket. This saddle is associated with the instability of each individual shear layer. The points at which the s_{2a} saddle exchanges dominance with the s_1 saddle can be seen at the intersection of their respective lines.

positions in $(x/t, z/t)$-space because the s_2 saddles asymptote to constant values of (ω, k). Along some rays, e.g. $(x/t, z/t) = (0.2, 0)$, both saddle points lie on the integration path and the response is a superposition of the short wavelength s_1 saddle and the long wavelength s_{2a} saddle.

Equation (2.8) becomes difficult to resolve numerically as δ tends to zero and generation of figures such as 4(*b*) becomes time-consuming. However, a quicker method can be used to generate a close approximation that is sufficiently accurate for this paper. An example is shown in figure 4(*c*). The unstable region of the s_1 saddle in $(x/t, z/t)$-space can be estimated by the region enclosed by its $g_i = 0$ contour, ignoring interactions with the s_2 saddles. This region asymptotes to a constant position as δ tends to zero and in this paper it is calculated for $\delta = 0.001$ using (2.8). This is

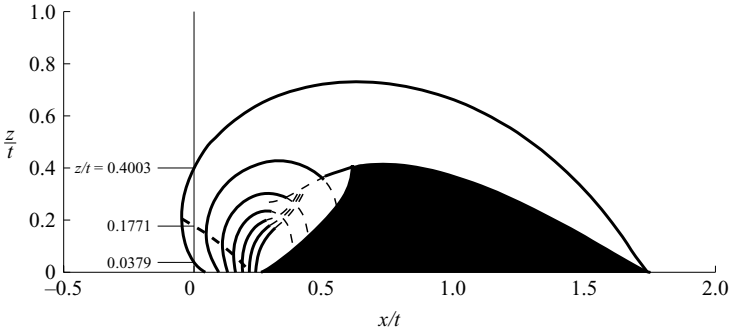

FIGURE 6. Contours of growth rate g_i representing the impulse response in the outer fluid for varicose perturbations of a flow with $(1/\Lambda, S) = (1.35, 0.03)$. Only the s_1 and s_{2a} saddle points are shown. This flow is convectively unstable, but on the line $x/t = 0$ the wavepacket has positive growth rate for z/t between 0.0379 and 0.4003 and maximum growth rate at $z/t = 0.1771$.

the black region. The growth rate contours of the s_{2a} saddle asymptote to constant values as δ tends to zero and these are calculated for $\delta = 0$ using (2.10). This saddle, shown by the thick black lines, dominates at the back and around the outside of the wavepacket. The s_{2b}, s_{2c}, s_{2d} etc. saddles dominate in the grey region and contribute to the integral (but do not dominate it) just upstream of this region. The exact structure of the contours in the grey region depends on δ: as δ decreases, higher-order s_2 saddles contribute to the integral and the complexity increases. The grey region does not have any influence on the effect being examined in this paper, so the simplified wavepacket in figure 4(c), without the grey region, is used.

5. Divergent eigenfunctions and saddle points that cross the k_i-axis

In § 4, it was shown that the long time behaviour of the impulse response can be determined from the behaviour of the saddle points in the k-plane. The aims of this section are to show that this remains the case when the s_{2a} saddle migrates into the plane of diverging eigenfunctions and to show that this does not violate Brigg's pinch criterion.

Figure 6 shows the impulse response for varicose perturbations of a flow with $(1/\Lambda, S) = (1.35, 0.03)$ as δ tends to zero. Along the thick dashed line at the back of the wavepacket, the s_{2a} saddle crosses the k_i-axis. Above this line, this saddle lies on the plane of converging eigenfunctions ($\xi_r > 0$) and the growth rate and amplitude of the impulse response decrease as z increases. Below this line, this saddle lies on the plane of diverging eigenfunctions ($\xi_r < 0$) and the growth rate and amplitude of the impulse response increase as z increases. The dashed line therefore corresponds to the point of maximum growth rate for a given x/t. For varicose perturbations in some low-density jets and sinuous perturbations in some high-density wakes this point lies off the x/t axis. Figure 6 is an example of such a flow. For instance, on the line $x/t = 0$ in figure 6, the wavepacket grows for z/t between 0.0379 and 0.4003, and the maximum growth rate is found at $z/t = 0.1771$.

It is unconventional to allow a saddle point to cross the k_i-axis, although Healey (2006) has shown that this is legitimate. For reassurance, the same result can be achieved without involving the plane of diverging eigenfunctions. In figure 7(a), contours of g_i are plotted in the k-plane for the ray $(x/t, z/t) = (0, 0)$ at the same

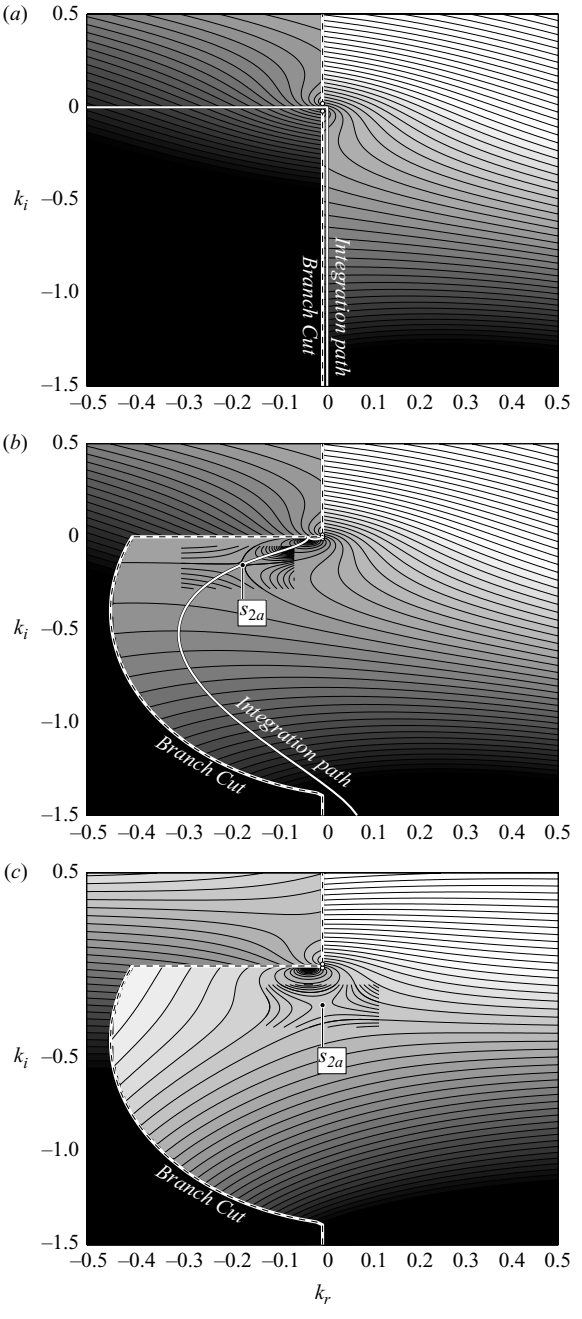

FIGURE 7. Contours of g_i in the k-plane for the flow in figure 6. (*a*) For the ray $(x/t, z/t) = (0, 0)$ on the plane of converging eigenfunctions ($\xi_r > 0$), which has a branch cut down the k_i-axis. A possible integration path is shown just to the right of this branch cut. (*b*) For the ray $(x/t, z/t) = (0, 0)$, moving the branch cut to allow the integration path to pass over saddle s_{2a}, which has migrated into the plane of diverging eigenfunctions. (*c*) For the ray $(x/t, z/t) = (0, 0.1771)$, which corresponds to the ray with highest growth rate on the line $x/t =, 0$ because saddle s_{2a} lies on the k_i-axis.

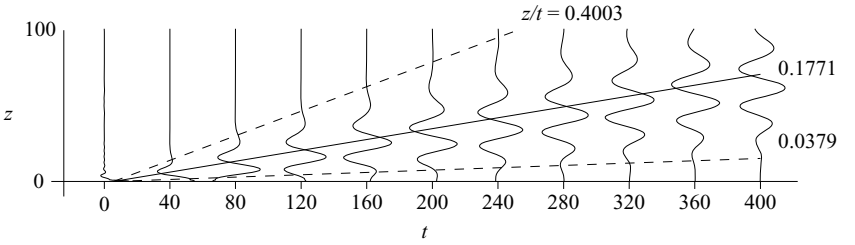

FIGURE 8. The impulse response in the plane $x/t = 0$ represented by the normalized pressure perturbation for the unconfined flow in figures 6 and 7. This has been calculated by integrating numerically over the path in figure 7(*a*), which is restricted to the plane of converging eigenfunctions. The centre of the wavepacket is at $z/t = 0.1771$.

parameter values as figure 6. There is a branch point near the origin at $-\mathrm{i}k_y$ and the branch cut from this point is normally placed along the negative k_i-axis, as described in § 2. The integration path is taken over the series of s_2 saddles and then the s_1 saddle. These are not shown in this figure, but can be seen in figure 3 for similar parameter values. If the path is to remain in the plane of converging eigenfunctions, it must take the path shown in figure 7(*a*) and pass over the ridge around $k = -0.3\mathrm{i}$, where the growth rate is positive.

This integration can be evaluated numerically and the impulse response can be represented conveniently by the normalized pressure perturbation $p(z, t)$ at $x = 0$ at successive times t. In this paper, 1000 points are taken on the path in the range $-1.57 < k_i < 0$, which encompasses all of the path that has positive g_i. The pressure perturbation is found from (5.1), which is the discrete form of the integral (3.9) at $x = 0$:

$$p(z, t) = \sum \frac{p(z; \xi)}{(\partial D/\partial \omega)[k, \omega(k)]} \mathrm{e}^{-\mathrm{i}\omega(k)t} \delta k. \tag{5.1}$$

The results are shown in figure 8. The wavepacket grows for z/t between 0.0379 and 0.4003, and has maximum growth rate at $z/t = 0.1771$, as expected from figure 6. Figure 6 was created using the procedure described next, which allows saddle s_{2a} to cross the k_i-axis.

The integration can be evaluated more easily by shifting the branch cut from the k_i axis, as shown in figure 7(*b*). This reveals saddle s_{2a}, which has migrated into the plane of diverging eigenfunctions. The integration path is deformed onto this saddle point, which is the highest saddle point on the integration path at these parameter values. This saddle point has negative g_i, which indicates that the response decays at $(x/t, z/t) = (0, 0)$. However, it is in the plane of diverging eigenfunctions, which indicates that the eigenfunction along the adjacent ray at higher z/t will have a higher growth rate. Both these features are in accordance with the previous numerical integration. It is important to note, however, that the present integration is not performed over the plane of divergent eigenfunctions that was eliminated in § 2 (the A-plane) because solutions on the path continue to satisfy $D^+ = 0$, rather than $D^- = 0$. The present process simply provides an easier method of performing the integral in the B-plane.

The same procedure is followed for non-zero $(x/t, z/t)$, moving into the plane of diverging eigenfunctions if necessary. The ray $(x/t, z/t) = (0, 0.1771)$ should correspond to the most highly amplified part of the wavepacket at $x/t = 0$. Contours of g_i are shown in figure 7(*c*) for this ray and, as anticipated, the s_{2a} saddle lies on

the k_i-axis. The phase velocity of this mode is in the z-direction and it is an example of a convective instability with growth normal to the shear layer, described by Healey (2006) for the rotating disk boundary layer.

5.1. *The k^+/k^- pinch criterion in the plane of diverging eigenfunctions*

At first sight, saddles in the plane of diverging eigenfunctions seem to violate the k^+/k^- pinch criterion of Briggs (1964). This requires that, for ω_i greater than the maximum temporal growth rate, the hill to one side of a saddle is confined to the $k_i > 0$ half-plane and the hill to the other side is confined to the $k_i < 0$ half-plane. For example, saddle s_{2a} in figure 7(b) is pinched between two hills that are both confined to the $k_i > 0$ half-plane at high ω_i and seems to be an invalid k^+/k^+ pinch point. The same result is found for the rotating disk boundary layer in saddle B of figure 5(a) in Healey (2006).

This potential complication is resolved by noticing that all branches behind the branch cut that usually lies on the negative k_i-axis have to be k^- branches, even if they move into the $k_i > 0$ half-plane at high ω_i and therefore look like k^+ branches. To be more specific, if the F_k integration in (3.5) is performed before the L_ω integration, the poles that are enclosed in the bottom half of the k-plane correspond to solutions for $x < 0$ and are called k^- branches. Similarly, the poles that are enclosed in the top half of the k-plane correspond to solutions for $x > 0$ and are called k^+ branches. This is a more general definition than examination of the behaviour of the hills on either side of the saddle. By definition, all saddle points on the integration contour are pinched between a k^- branch and a k^+ branch. When the integration path is deformed through the branch cut on the negative k_i-axis, as in figure 7(b), a k^+ branch hits a saddle point on the plane of diverging eigenfunctions. The branch on the other side of the saddle point must be a k^- branch because it is always closed in the bottom half of the k-plane, even if the branch moves into the $k_i > 0$ half-plane as ω_i increases.

In conclusion, examining the hills on either side of a saddle does not safely indicate the validity of a saddle point in the plane of diverging eigenfunctions and it is better to consider the whole integration path.

6. Effect of density ratio on varicose perturbations of unconfined shear flows

The aim of this section is to use the processes developed in previous sections to characterize the behaviour of unconfined jets and wakes over large variations of the density ratio and shear number. The impulse response is evaluated for varicose perturbations of a low-density jet. The equivalent region for sinuous perturbations can be evaluated directly under the transformation $(\mathrm{var}, 1/\Lambda, S) \leftrightarrow (\sin, -1/\Lambda, 1/S)$.

The boundaries of absolute and convective instability in the $(1/\Lambda, S)$-plane are shown at the centre of figure 9. This figure is calculated in the same way as figure 6 of Juniper (2006) and figure 2 of Yu & Monkewitz (1990). However, saddle points are allowed to cross the k_i-axis and this provides the correct characterization below the dashed line. The dashed line corresponds to the points where the s_{2a} saddle lies on the k_i-axis for the ray at $(x/t, z/t) = (0, 0)$. The impulse response in the outer fluid is shown at selected points in the surrounding figures. The impulse responses all have the features described in § 4: the s_1 saddle dominates in the centre of the wavepacket (black region), corresponding to the instability of each individual shear layer, and the s_{2a} saddle dominates at the back of the wavepacket, corresponding to the varicose instability of the interacting shear layers. As S decreases, the bulge at the back of the wavepacket becomes more distinct and as $1/\Lambda$ increases, the wavepacket shifts

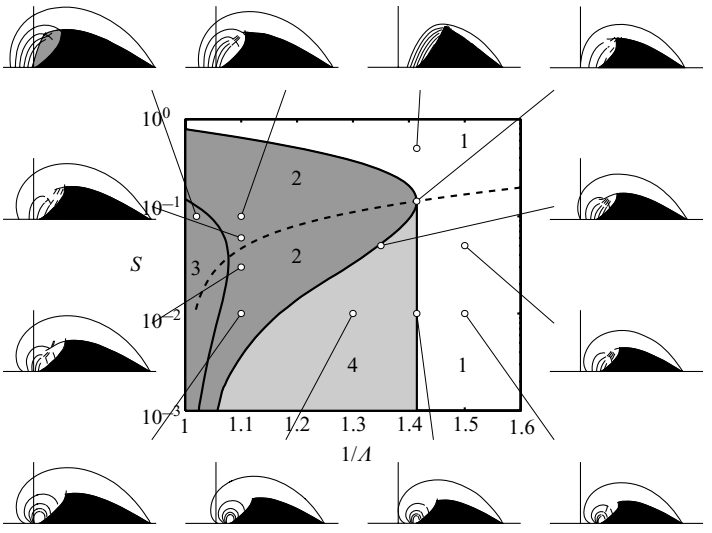

FIGURE 9. Central figure: absolutely unstable (dark grey) and convectively unstable (light grey and white) regions of the $(1/\Lambda, S)$-plane for varicose perturbations of a low-density unconfined coflow jet. Surrounding figures: impulse responses in the outer fluid, using the same scales as figures 3 and 6. Only the contributions of the s_1 and s_{2a} saddles are shown, except in the top left-hand figure where the region affected by the s_{2b} saddle is also shown.

downstream with little change in shape. There are five distinct regions of the plane, distinguished by the behaviour along the rays with $x/t = 0$ of the impulse responses (i.e. the z/t axes).

Region 1 is convectively unstable because the growing wavepacket propagates downstream and all the eigenmodes with zero group velocity in the x-direction decay. Above the dashed line, the mode with highest growth rate and with $x/t = 0$ also has $z/t = 0$. Below the dashed line, the mode with highest growth rate and with $x/t = 0$ has positive z/t. However, this has no consequence in region 1 because all modes on rays with $x/t = 0$ decay.

Region 2 is absolutely unstable because the eigenmode with zero group velocity, $(x/t, z/t) = (0, 0)$, grows. Above the dashed line, the mode with highest growth rate and with $x/t = 0$ is found at $z/t = 0$. Below the dashed line, the mode with highest growth rate and with $x/t = 0$ is found at $z/t > 0$. However, this has little consequence in region 2 because the flow is always absolutely unstable. The wavepacket in figure 3(c), with $(1/\Lambda, S) = (1.1, 0.1)$ is in region 2.

Region 3 is similar to region 2, but is also absolutely unstable to the s_{2b} saddle. The wavepacket looks like that in region 2, but is shifted upstream so that the s_{2b} saddles contribute at the point of impulse rather than just downstream of this point.

Region 4, which has not been recognized previously, contains the type of impulse response described in § 5. It is convectively unstable because the mode with zero group velocity, $(x/t, z/t) = (0, 0)$, decays. However, parts of the growing wavepacket propagate upstream, at an angle to the flow direction, and this has important consequences for confined flows, as described in § 7. This region extends up to $1/\Lambda = \sqrt{2}$, a result derived in the Appendix.

Region 5 is not shown in figure 9, but lies in the region of counter flow, for which $-1 < 1/\Lambda < 1$. In this region, saddle s_1 can have positive growth rate at $(x/t, z/t) = (0, 0)$ and the individual shear layers can be absolutely unstable. In other

words, the black region can extend either side of the point of impulse. The varicose interacting mode can also be absolutely unstable, and these regions are shown in figure 6 of Juniper (2006), but this mode always has lower growth rate than the s_1 saddle.

This concludes the first aim of the present paper: to re-examine unconfined jets and wakes without discounting eigenmodes with negative k_r.

7. Implications for confinement

The second aim of the present paper is to re-examine the effect of confinement on inviscid jets and wakes. This can now be fully understood by considering the characteristics of the regions defined in § 6. In region 4 of figure 9, flows are convectively unstable when unconfined and absolutely unstable when confined, even as h tends to infinity. This can be explained both mathematically, by consideration of the ω_i contours in k-space for the ray $(x/t, z/t) = (0, 0)$, and physically, by consideration of the shape of the growing wavepacket. In both cases, it is only necessary to consider the case with infinitely thin shear layers because all the relevant behaviour is due to the s_{2a} saddle. In this section, the wavepacket shown in figure 6 is considered with the confining wall placed at $h = 100$.

Mathematically, confinement introduces a factor of $\coth \xi h$ into the dispersion relation, as seen by comparing (2.12) with (2.13). This creates a series of branch points and poles on the k_i-axis, as described by Juniper (2006) for jets and wakes and by Healey (2007) for the rotating disk boundary layer. These poles create a series of saddle points with k_r of order $1/h$, over which the integration contour must pass (figure 10). If, in the unconfined case, the $\omega_i = 0$ contour crosses the k_i-axis then, in the confined case, at least one of the new series of saddle points must have ω_i greater than zero. This means that the confined flow is absolutely unstable, even though the equivalent unconfined flow is convectively unstable. This remains true as h tends to infinity because the branch points become closer together on the k_i-axis. The branch cut cannot be deformed away from the k_i-axis, as it was for the unconfined case, owing to this series of branch points on the k_i-axis. Healey (2007) found this behaviour in the confined rotating disk boundary layer and, in the current paper, the same behaviour is found in confined jets and wakes. In figure 10, the pressure eigenfunction of the most unstable saddle point is shown in the inset. It has a positive growth rate.

Physically, this can be understood by considering the shape of the growing wavepacket in figure 6 and remembering that a flow is defined as absolutely or convectively unstable only in the long time limit. Although the mode with zero group velocity, at $(x/t, z/t) = (0, 0)$, decays, the wavepacket contains growing eigenmodes along rays with $x/t = 0$ and positive z/t. These cause the growth away from the shear layer that is seen in figure 8. The wavepacket travels in the positive z-direction and, for the confined flow, reflects off the wall and travels back in the negative z-direction. This eventually sets up a standing wave in the $x = 0$ plane, as can be seen in figure 11, which is calculated in the same way as figure 8. Of course, the shape of the standing wave is that of the most unstable saddle point in the k-plane (figure 10), which gives the behaviour in the long time limit. This standing wave, like its component waves, has positive growth rate and is therefore absolutely unstable.

In Juniper (2006) the saddle points shown in figure 10 were called 'ambiguous' at large h and were discounted because they have small k and do not predict the same behaviour as the unconfined case when h tends to infinity. However, the mathematical

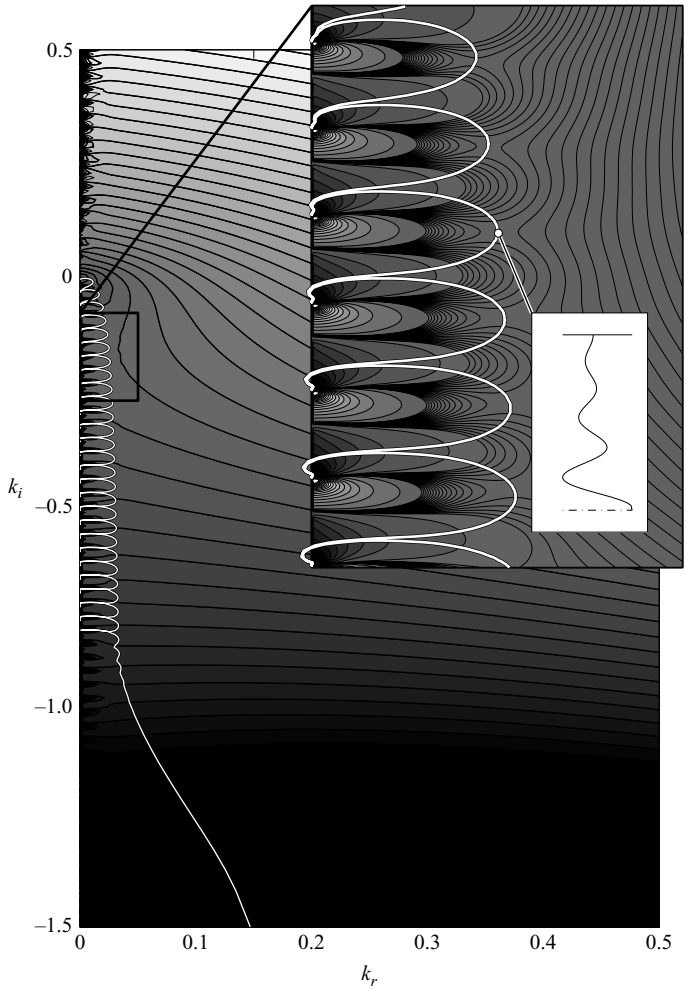

FIGURE 10. Contours of g_i in the k-plane for varicose perturbations of a confined flow with $(1/\Lambda, S, h) = (1.35, 0.03, 100)$, which is at the same shear and density ratio as the unconfined flow in figure 7(a). Poles and branch points on the k_i-axis prevent the integration path from crossing the k_i-axis as in figure 7(b) and the path traverses a series of saddle points near this axis (inset figure). The most unstable saddle point has positive growth rate and its mode shape is shown.

and physical arguments in this section and in Healey (2007) demonstrate why these saddles should not, in fact, be discounted. Under the conditions in region 4 of figure 9, a jet flow will be linearly convectively unstable when unconfined and linearly absolutely unstable when confined. Furthermore, the flow is always absolutely unstable to saddle s_1 in region 5, where $-1 < 1/\Lambda < +1$. Although Juniper (2006) shows that 'ambiguous' saddles exist at these values of $1/\Lambda$, they are more stable than the s_1 saddles and their effect on absolute/convective transition in the flow can be ignored.

Regions 1, 2 and 3 in figure 9 do not contain this type of saddle point and the confined case with h tending to infinity gives the same result as the unconfined case. However, confinement with $h \sim 1$ has a strong effect on these flows when the z-wavenumbers, k_i, of modes with zero group velocity in the outer flow match those of the inner flow. This is described in Juniper (2006).

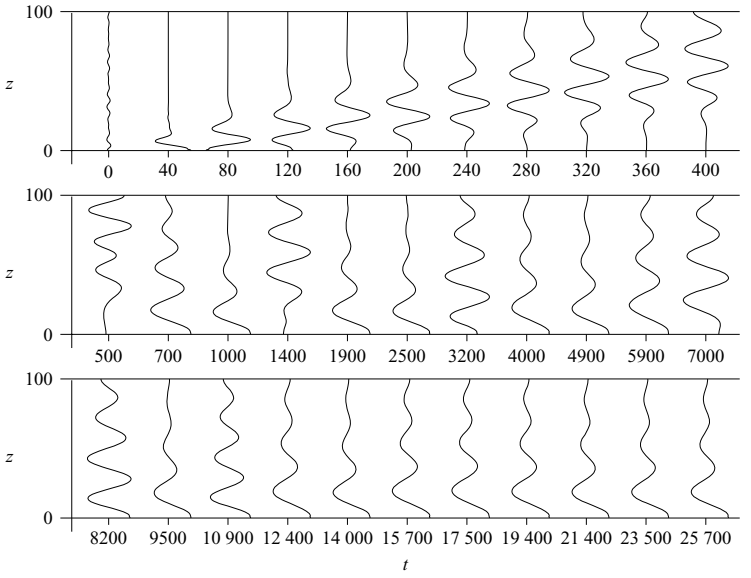

FIGURE 11. The impulse response in the plane $x/t = 0$ represented by the normalized pressure perturbation for the confined flow in figure 10. The top series is similar to figure 8, which represents the equivalent unconfined flow. The subsequent plots show how the impulse response reflects off the boundary and sets up a standing wave with the mode shape of the most unstable saddle point in figure 10.

As a final point, the behaviour of a weakly confined flow (i.e. large h) is unlikely to be predicted well by this analysis when the flow evolves in the x-direction more quickly than order h. This is because the apparent wave propagation in the z-direction in the outer fluid, which is the origin of this curious behaviour, is simply a response to the perturbation at the shear layer. Consequently, it is reasonable to expect that the response at $z = h$ receives contributions from a region of the shear layer of streamwise length of order h. If the base flow evolves more quickly than this, the response at $z = h$ is likely to be inaccurate.

8. Conclusions

A linear spatio-temporal stability analysis is performed on a simple model jet/wake flow in order to discover whether it has similar characteristics to the rotating disk boundary layer studied by Healey (2006). The impulse response is evaluated by integrating over a path in the complex k-plane. Particular attention is paid to this path and to the positions of branch cuts in the k-plane. The first set of conclusions concerns this process. In the unconfined case, the contribution from the plane of diverging eigenfunctions (the A-plane) must be zero. However, when integrating over the plane of converging eigenfunctions, it is legitimate to pass into a small region of diverging eigenfunctions. This integration is not the same as that over the plane of diverging eigenfunctions that was previously rejected. For reassurance, the same result can be derived by integrating numerically over the plane of converging eigenfunctions alone.

The impulse response for unconfined flows is evaluated throughout the outer fluid, rather than just at the point of impulse. The second set of conclusions concerns this full impulse response. The impulse in this paper is centred at $(x, z, t) = (0, 0, 0)$, but

excites all eigenfunctions equally, rather than being concentrated at the shear layer, $z=0$. Although this impulse takes the form of a doublet, the response is the same as that of a point source at $z=0$. This is because of the constraints of incompressibility and irrotationality. There is no dynamic constraint in the outer flow so, at $t>0$, the outer flow has no memory of the initial impulse except through its kinematic response to the shear layer, which is affected only by the impulse at $z=0$. The response consists of eigenmodes propagating at different group velocities. Eigenmodes with diverging eigenfunctions are permitted and simply correspond to regions of the wavepacket for which the growth rate increases as z increases. These regions arise when the dominant saddle point lies on the plane of diverging eigenfunctions mentioned in the previous paragraph. This demonstrates that the unconfined jet/wake flow behaves in a similar manner to the unconfined rotating disk boundary layer studied by Healey (2006). These regions are all associated with the interaction of the two shear layers rather than the behaviour of each individual shear layer.

By examining the response in the whole outer fluid, rather than just at the point of impulse, a set of conclusions can be drawn for unconfined jet/wake flows. The absolutely unstable region of the $(1/\Lambda, S)$-plane is bigger than previously thought (it includes the bottom half of region 2 in figure 9). There is a region of the $(1/\Lambda, S)$-plane where parts of the wavepacket propagate and grow upstream, even though the response decays at the point of impulse (region 4 in figure 9). The impulse response has a similar shape over a wide range of $1/\Lambda$ and S, although the region with diverging eigenfunctions becomes larger as S becomes further from 1.

Considering the impulse response for unconfined flows reveals a further set of conclusions for confined flows. Confinement has little effect on the stability of most flows unless the inner and outer flows have comparable widths ($h\sim 1$) (Juniper 2006). However, flows in region 4 of figure 9 are convectively unstable when unconfined and absolutely unstable when confined. This is because, even though the response decays initially at the point of impulse, part of the wavepacket propagates and grows in the z-direction, reflects off the confining wall and then sets up a growing standing wave in the outer fluid.

This paper demonstrates that confinement can destabilize inviscid jets and wakes in the same way that it destabilizes the rotating disk boundary layer in Healey (2007). Together with Juniper (2006), this paper reveals the full influence of the density ratio combined with confinement. It is particularly significant for fuel injection systems, which often involve confined shear flows at high Reynolds numbers and large density ratios.

Appendix. Evaluating the boundary of region four

On the boundary of region 4 in figure 9, the contour with $\omega_i=0$ on the k^+ branch just touches the k_i-axis. Consequently, the parameter values that define this boundary can be found by searching for a two-fold degenerate root to $\omega_i=0$ on the negative k_i-axis.

Equation (2.12) can be re-arranged so that ω is an explicit function of k:

$$\frac{\omega}{k}=1+\Lambda\frac{1+f}{1-f}\qquad\text{where}\qquad f\equiv\pm\left(-\frac{\tanh k}{S}\right)^{1/2}. \tag{A 1}$$

The wavenumber, k, is given by $k=-\mathrm{i}k_i$, where k_i is a positive real number. The function f can then be expressed as $f\equiv\pm(\mathrm{i})^{1/2}g$, where g is the real number $(\tan k_i/S)^{1/2}$. The fourth power of f is a real number and (A 1) can be rearranged

such that the denominator is real and the numerator contains all the imaginary components:

$$\frac{\omega}{-\mathrm{i}k_i} = 1 + \Lambda \frac{1 + 2f + 2f^2 + 2f^3 + f^4}{1 - f^4}. \tag{A 2}$$

The real part of the right-hand side of (A 2) must be zero because $\omega_i = 0$. The real components of f, f^3 and f^4 can be substituted into (A 2) to give:

$$g^4(1 - \Lambda) + (g - g^3)\Lambda\sqrt{2} + (1 + \Lambda) = 0, \tag{A 3}$$

which has solutions:

$$g = -\frac{1 \pm \mathrm{i}}{\sqrt{2}}, \quad g = \frac{-1 \pm \sqrt{2\Lambda^2 - 1}}{\sqrt{2}(\Lambda - 1)}. \tag{A 4}$$

When $\Lambda = 1/\sqrt{2}$, there is a two-fold degenerate solution with $g = 1 + \sqrt{2} = 2.4142$. At this value of Λ, the k^+ branch with $\omega_i = 0$ just touches the k_i-axis at $k_i = \tan^{-1}(gS)$. This marks the boundary of region 4.

REFERENCES

Barrère, M. & Jaumotte, A. & Fraeijs de Veubeke, B. & Vandenkerckhove, J. 1960 *Rocket Propulsion*. Elsevier.

Briggs, R. J. 1964 Electron-stream interaction with plasmas. M.I.T. Press.

Chen, J.-H., Pritchard, W. G. & Tavener, S. J. 1995 Bifurcation for flow past a cylinder between parallel planes. *J. Fluid Mech.* **284**, 23–41.

Delbende, I. & Chomaz, J.-M. 1998 Nonlinear convective/absolute instabilities in parallel two-dimensional wakes. *Phys. Fluids* **10**(11), 2724–2736.

Drazin, P. & Reid, W. 1981 *Hydrodynamic Stability*. Cambridge University Press.

Esch, R. E. 1957 The instability of a shear layer between two parallel streams. *J. Fluid Mech.* **3**, 289–303.

Garcia-Villalba, M., Fröhlich, J. & Rodi, W. 2006 Numerical simulations of isothermal flow in a swirl burner. *ASME Turbo Expo* GT2006-90764.

Healey, J. J. 2006 A new convective instability of the rotating-disk boundary layer with growth normal to the plate. *J. Fluid Mech.* **560**, 279–310.

Healey, J. J. 2007 Enhancing the absolute instability of a boundary layer by adding a far-away plate. *J. Fluid Mech.* **579**, 29–61.

Huerre, P. 2000 Open shear flow instabilities. In *Perspectives in Fluid Dynamics : A Collective Introduction to Current Research* (ed. G. K. Batchelor, H. K. Moffat & M. G. Worster). Cambridge University Press.

Juniper, M. P. 2006 The effect of confinement on the stability of two-dimensional shear flows. *J. Fluid Mech.* **565**, 171–195.

Juniper, M. P. & Candel, S. M. 2003 The stability of ducted compound flows and consequences for the geometry of coaxial injectors. *J. Fluid Mech.* **482**, 257–269.

Shair, F. H. & Grove, A. S. & Petersen, E. E. & Acrivos, A. 1963 The effect of confining walls on the stability of the steady wake behind a circular cylinder. *J. Fluid Mech.* **17**, 546–550.

Yu, M.-H. & Monkewitz, P. A. 1990 The effect of nonuniform density on the absolute instability of two-dimensional inertial jets and wakes. *Phys. Fluids* A **2**(7), 1175–1181.